Chinese Chemical Letters 35 (2024) 108449

Contents lists available at ScienceDirect

Chinese Chemical Letters

journal homepage: www.elsevier.com/locate/cclet

# Rocking-chair ammonium ion battery with high rate and long-cycle life

Tongkai Wang[a,1], Xiaojuan Li[a,1], Shunshun Zhao[b], Hongxia Bu[c,*], Chuanlin Li[a], Na Li[a], Xixi Zhang[a], Xijin Xu[a,*]

[a] School of Physics and Technology, University of Jinan, Ji'nan 250022, China
[b] State Key Laboratory of Chemical Resource Engineering, Beijing Key Laboratory of Electrochemical Process and Technology of Materials, Beijing University of Chemical Technology, Beijing 100029, China
[c] College of Physics and Electronic Engineering, Qilu Normal University, Ji'nan 250200, China

ARTICLE INFO

*Article history:*
Received 2 February 2023
Revised 18 March 2023
Accepted 12 April 2023
Available online 13 April 2023

*Keywords:*
Copper hexacyanoferrate
Vanadium-based compounds
Aqueous ammonium ion batteries
Long-term cyclability
Ammonium ion storage mechanism

ABSTRACT

Aqueous rechargeable ammonium-ion batteries (AIBs) have drew considerable attention because of their capacity for high rates, low cost, and high safety. However, developing desired electrodes requiring stable structure in the aqueous fast ammoniation/de-ammoniation becomes urgent. Herein, an ammonium ion full battery using $Cu_3[Fe(CN)_6]_2$ (CuHCF) acting to be a cathode and barium vanadate (BVO) acting to be an anode is described. Its excellent electrochemical behavior of Prussian blue analogs and the perfectly matched lattice structure of $NH_4^+$ is expected. And the open structure of vanadium compounds satisfies the fast ammoniation/de-ammoniation of $NH_4^+$ is also achieved. As a result of these synergistic effects, the BVO//CuHCF full cell retains 80.5 percent of its capacity following 1000 cycling. These achievements provide new ideas for developing low-cost and long-life AIBs.



Currently, batteries made of lithium-ion in commercial use are used in many portable electronic devices and electric vehicles (EVs) increased costs due to the intensified development of lithium resources [1,2]. Even so, using flammable and toxic organic electrolytes raises safety and environmental problems. Therefore, rechargeable aqueous batteries with inexpensive costs and high safety have gained considerable attention, particularly for large-scale energy storage systems [3]. The metal ions $K^+$, $Na^+$, $Li^+$, $Mg^{2+}$, $Zn^{2+}$, $Ca^{2+}$ and $Al^{3+}$ are usually used as a carrier in most rechargeable aqueous batteries [4–10]. As carriers of charge within aqueous batteries, nonmetallic cations, such as ammonium hydrate as well as ammonium ions, were rarely investigated [11].

The non-metallic carriers have the advantages of small molar mass, small hydration mass, rich resources and no dendrite compared with metal ions [12]. In comparison with other metal ions, the ionic radius for $NH_4^+$ is greater than 1.48, but the hydration radius of ammonium ion is only 3.31 Å [13–15]. The small hydrated ion radius and light mass facilitate the rapid diffusion of $NH_4^+$ in aqueous electrolytes. Ammonium ions are less corrosive and hydrogen precipitated than other nonmetallic cations [16]. The utilization of the $NH_4^+$ electrolyte acid base is moderate, and the corrosion of the electrode is weak, building a neutral or weak acidic environment with reduced hydrogen evolution side reactions. Besides, the abundant ammonium ion carrier minimizes the cost of ammonium ion batteries (AIBs) [17–20]. Consequently, AIBs have a promising prospect in large-scale energy storage and smart grid [11,21].

In the process of charging and discharging in AIBs, ammonium ions move back and forth between the positive and negative electrodes. AIBs is like a rocking chair, with the ends of the chair being the poles of the battery, and the ammonium ions are like running back and forth with the rocking chair [22,23]. The performance of the electrode material is a decisive factor for the performance of rocking chair battery, so higher requirements are put forward for the electrode. Prussian blue is referred to as PB, while Prussian blue analogs are referred to as PBAs as positive electrodes in rechargeable aqueous batteries. They have been reported due to their superior electrochemical properties and open 3D frame structures [22–24]. PB and PBAs have the common structural equation $A_2M[M'(CN)_6]$ (A is equal to Ions of alkaline metals; M/M' is equal to Fe, Cu, Co, and so on), in which other transition metal ions can replace metal ions, and further enrich kinds of PB and PBAs [25]. For example, Wu *et al.* explored a $K_{0.02}Ni_{1.45}[Fe(CN)_6]_2{\cdot}6H_2O$ as the positive electrode of an aluminum ion battery. They found

* Corresponding authors.
*E-mail addresses:* buhx666@163.com (H. Bu), sps_xuxj@ujn.edu.cn (X. Xu).
[1] These authors contributed equally to this work.

https://doi.org/10.1016/j.cclet.2023.108449
1001-8417/

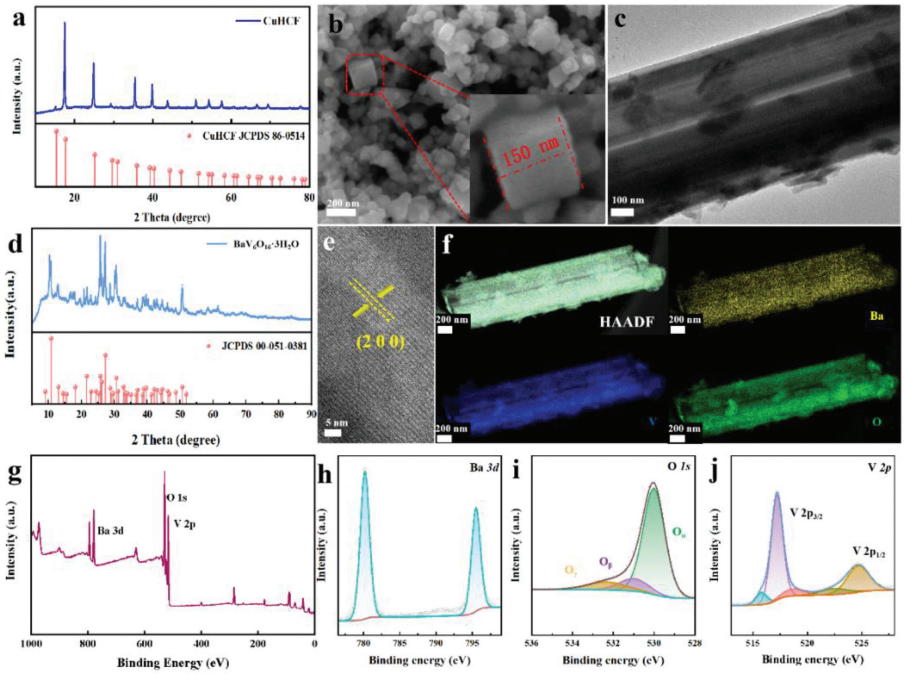


**Fig. 1.** (a) XRD image and (b) SEM image of CuHCF. (c) TEM images for BVO. (d) XRD images and (e) HRTEM images for BVO. (f) HAADF and EDS elemental mappings of BVO nanobelts, showing clearly the homogeneous distribution of and Ba, V and O. XPS spectra of different elements for (g) all elements, (h) Ba, (i) O, and (j) V elements.

that the capacity compensation effect was used in aluminum ion removal. The dissolution of trace Ni could promote Fe to contribute more capacity without causing sharp capacity decay [26]. In addition, $KMnFe(CN)_6{\cdot}nH_2O$ prepared by Lou *et al.* were applied to aqueous zinc ion batteries. By cosubstituting, the Mn-$N_6$ octahedron would not undergo Jahn-Teller distortion. Jiang *et al.* used $K_xFe_yMn_{1-y}[Fe(CN)_6]_w{\cdot}zH_2O$ to be the positive electrode in the stream potassium ion battery, and Fe replaced part of Mn, which improved the cycling performance, electron and ion conductance and performance of rate of the positive electrode [27]. Nanofiltration and PBAs Materials are used to store Nanofiltration $NH_4^+$. Xia *et al.* prepared an AIBs with $K_{2.04}Ni_{0.98}[Fe(CN)_6]{\cdot}1.88H_2O$ as the positive electrode poly(1,5-NAPD) as the negative electrode 19 mol/L $CH_3COONH_4$ as the electrolyte, achieving −40 °C to 80 °C work in a wide temperature range [16]. PBAs have zero-strain characteristic $NH_4^+$ of insertion, so they have very broad prospects in AIBs.

Anodes for AIBs have been developed from transition metal oxides, sulfides, and organic compounds. Transition metal oxides/sulfides allow $Li^+$, $Na^+$ and $K^+$ to be inserted and removed at low potentials. Organic compounds can accommodate $NH_4^+$ due to their large internal voids and stable structure [28]. Due to their open frame structure, vanad-based materials have attracted considerable attention, which can accommodate many kinds of ions [29–31].

In this work, the CuHCF cathode exhibits a specific capability of 66.2 mAh/g at 1 A/g, maintaining a good retention of capability (77%) following 3500 cycles. $BaV_6O_{16}{\cdot}3H_2O$ anode possesses a high capacity for discharge of 138.54 mAh/g. As a result, AIBs using $Cu_3[Fe(CN)_6]_2$ (CuHCF) as positive and $BaV_6O_{16}{\cdot}3H_2O$ as negative present its high power density as well as its ability to last for a long time. The study provides new insight into building high-performance AIBs.

CuHCF prepared by coprecipitate method has shown high crystallinity and purity by X-ray diffraction (XRD) spectrogram analysis. CuHCF and standard comparison card (JCPDS No. 86–0514) has extraordinary coincidence. Scanning electron microscopy (SEM) image of CuHCF is shown in Fig. 1a, which presents a dispersive nanoparticle. The majority of particles have a cubic structure. There is a similar distribution of cubic boxes to that of a random distribution. There is uniform dispersion of nanoparticles throughout the field of view, and they retain their cubic morphology. Based on the inset of Fig. 1b, CuHCF particles have a side length of approximately 150 nm. Using a simple hydrothermal process, BVO was synthesized in one step. According to transmission electron microscopy (TEM) images, BVO has a multi-level prism morphology (Fig. 1c), with a transparent texture of the smooth and uniform surface. The XRD pattern of BVO (Fig. 1d) can correspond well to $BaV_6O_{16}{\cdot}3H_2O$ (JCPDS No. 51–0381). High-resolution TEM (HRTEM) images of BVO show lattice-resolved streaks at a distance of 0.608 nm from the (200) crystal plane (Fig. 1e). A scanning transmission electron microscope (Fig. S1 in Supporting information), an energy dispersive X-ray elemental mapping (Fig. 1f) as well as spectra (Fig. S2 in Supporting information) revealed that Ba, V and O are uniformly distributed on BVO. Fig. 1g is the X-ray photoelectron spectroscopy (XPS) total spectrum showing elements Ba, O and V. $Ba^{2+}$ is bonded to oxygen atoms in BVO, and the original electrode only shows the Ba 3d component (Fig. 1h). In the O 1s region (Fig. 1i), the three peaks at the binding energy of 530, 531 and 532.4 eV form lattice oxygen bonds with V ($O_\alpha$), surface adsorbed oxygen ($O_\beta$, *i.e.*, $O^{2-}$, $O^-$ and OH groups) as well as the inserted $H_2O$ molecule ($O_\gamma$), accordingly [32]. Meanwhile, a pair of peaks located at 517.3 eV and 524.6 eV are associated with the spin-orbits of V $2p_{3/2}$ and V $2p_{1/2}$, respectively (Fig. 1j) [32,33].

Based on a rate of scan of 1 mV/s, Fig. 2a indicates the curves for voltammetry cyclic of CuHCF cathode. A redox couple of reduction and oxidation peaks is located at 0.73 and 0.81 V, which is consistent with the ammonia/deamination process of CuHCF. Fig. 2b illustrates CV curves at various scanning rates. When the rates of scan rise from 1 mV/s to 50 mV/s, its peaks of reduction change to higher voltages and its peaks of oxidation change to lower voltages, indicating aggravated electrochemical polarization. Fig. 2c illustrates the charge and discharge curves of CuHCF under a range of current densities. The current density range of 1, 2, 5, 8, 10, 15,

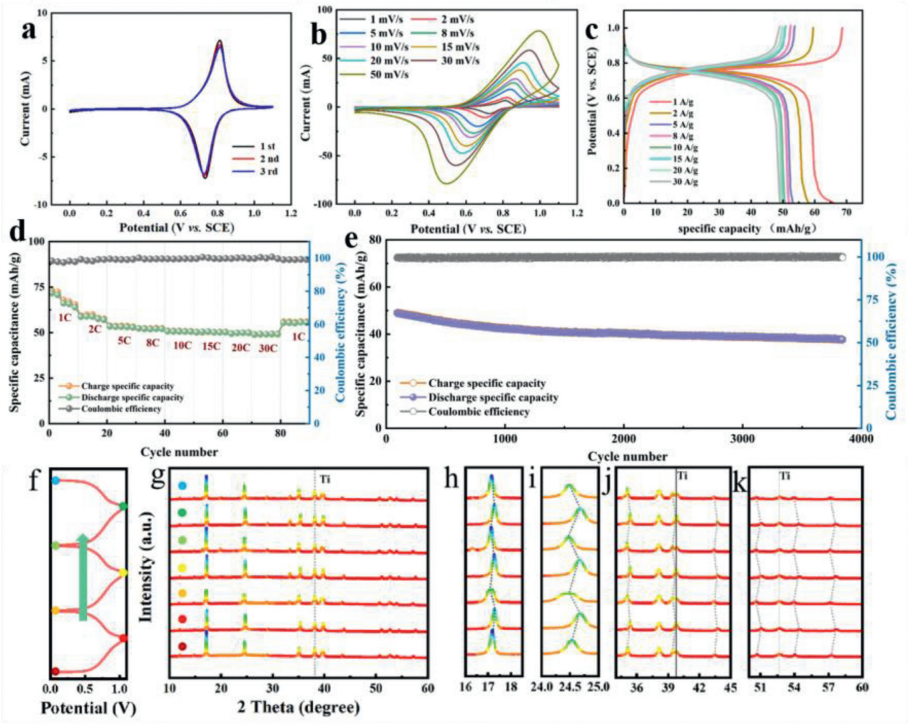


**Fig. 2.** Electrochemical properties of the CuHCF cathode. (a) CV plots for the first three cycles at 1 mV/s. (b) CV curve at different scan rates. (c) Galvanostatic charge–discharge curves at different current densities. (d) Rate performance is between 1 C and 30 C. (e) Long-term cycle performance at a high current rate of 10 C. (f) The charge/discharge curve for the CuHCF electrode. Sampling points for XRD pattern were marked with the corresponding colored dots. (g) *Ex-situ* XRD patterns, and (h-k) the magnified XRD patterns of different peaks.

20 and 30 A/g provides specific capacities of 66.2, 58.1, 53.2, 52.1, 50.6, 50, 49.6 and 49.2 mAh/g. Fig. 2d shows the CuHCF cathode has excellent rate performance between 1 C and 30 C. Fig. 2e illustrates the high cycling efficiency of the CuHCF cathode at the current rate of 10 C, remaining at 77% after 3500 cycles. *Ex-situ* XRD analysis is performed in order to examine the structural evolution of CuHCF electrodes during ammonium ion ammoniation/deammoniation.

The charge and discharge curves of CuHCF and their corresponding XRD patterns are shown in Figs. 2f and g. After several cycles, no other impurity phases are generated, and CuHCF maintains a cubic structure. As shown in the enlarged images of various crystal planes (Fig. 2h, (200); Fig. 2i (220); Fig. 2j (400), (420), (422); Fig. 2k (440), (442), (620)), after several times undergoing charging and discharging, all crystal has the same evolution trend, in the process of ammoniation (discharge) diffraction peak to large angle offset, deamination (charge) in the process of the diffraction peak again to go back to the previous position [34].

Fig. 3 shows the $NH_4^+$ storage performance of BVO evaluated at 1 mol/L $(NH_4)_2SO_4$. Fig. 3a indicates the CV curves for BVO at various current densities. Fig. 3b shows the rate of discharge of the BVO anode, which provides a discharge capacity of 138.54, 101.04, 81.42 and 54.56 mAh/g at 0.5, 0.8, 1 and 2 A/g, accordingly. The electrochemical impedance spectroscopy (EIS) of BVO consists of semi-circles for the high-frequency region as well as bending lines for the low-frequency region (Fig. S3 in Supporting information). For the region with a low frequency, its BVO spectrum's linear slope is ~50°, which confirms the diffusivity of the controlled ion diffusion efficiency within the electrolyte in the redox reaction. In addition, the specific contributions of the capacitance behavior ($k_1v$) and the diffusion control insertion ($k_2v^{1/2}$) were calculated based on $i = k_1v + k_2v^{1/2}$ (Fig. 3c) [35–37]. When the scan rate is as low as 0.1 mV/s, approximately 14% of the total charge stored is accounted for by capacitance. But as the scanning rate rises to 2 mV/s, the percentage increases to around 75%. These results confirm that energy storage in BVO is generated by $NH_4^+$ diffusion. The cycle performance at 1 C ratio is shown in Fig. S4 (Supporting information). The battery contains a reversible capability of 30.2 mAh/g following 200 cyclings and retains 40% of its capacity after 200 cycles. However, the capacitance shows a rapid decrease after 200 cycles, most likely due to the escape of water molecules from the interlayers during the deep charge–discharge cycle [33].

At the same time, we also carried out the same study on the negative electrode of BVO, and combined with the XRD pattern amplification of various crystal faces. It was obvious that with the charging and discharging process (Fig. 3d), BVO (002) (004) (303) (006) crystal faces had various evolution trends (Fig. 3e), in which (002) (004) crystal faces expanded slightly with ammonium ion intercalation (Figs. 3f and g). In addition, the crystal plane contracted with the release of ammonium ion. In contrast, in the (303) (006) crystal plane (Figs. 3h and i), the diffraction peak moved to a large angle with the discharge process, because the inserted $NH_4^+$ not only formed an H bond with the O generated by the adjacent BVO, but also formed a hydrogen bond with the adjacent lattice water [33].

Fig. 4 studies the electrochemical properties of the BVO//CuHCF full cell assembled under anodic capacity constraints, where the ammonium ion shuttles reversibly between the BVO anode and the CuHCF cathode. To further investigate the electrochemical reversibility and dynamics of the whole cell, CV tests are performed using various scanning rates of 2–50 mV/s in Fig. 4a. These curves do not deform significantly as the rates of scan increase, which shows that the BVO//CuHCF cell exhibits good reaction kinetics. An analysis of the association involving peak current and the scan rate was conducted to further investigate the response properties according to Eq. 1 [38–40].

$$i = av^b \quad (1)$$

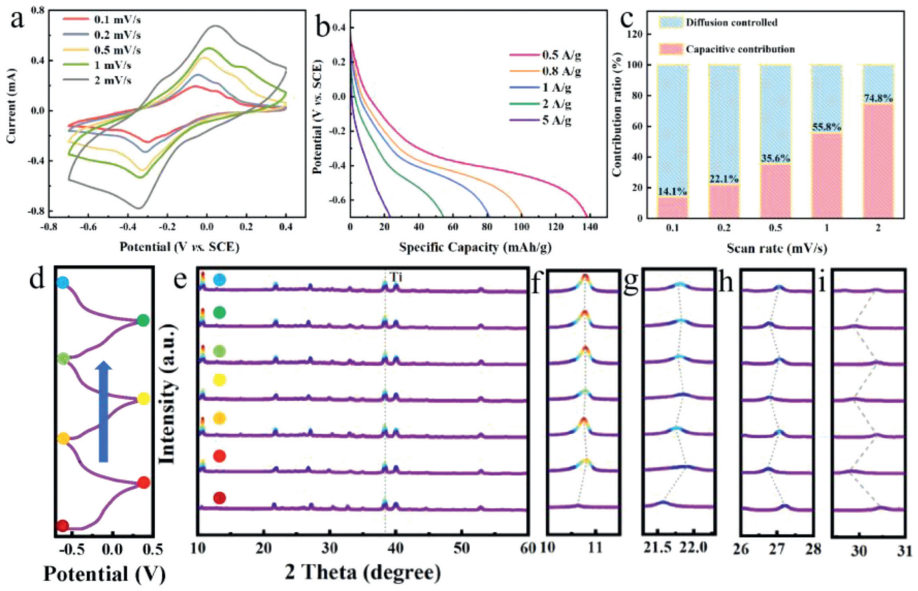


**Fig. 3.** Electrochemical properties of the BVO cathode. (a) CV curve at different scan rates. (b) Galvanostatic discharge curves at various current densities. (c) The contribution rate of capacitance and diffusion control performance at different scanning rates. (d) The charge/discharge curve for the BVO electrode. Sampling points for XRD pattern were marked with the corresponding colored dots. (e) *Ex-situ* XRD patterns. (f-i) The magnified XRD patterns of (002), (004), (303) and (006) peaks.

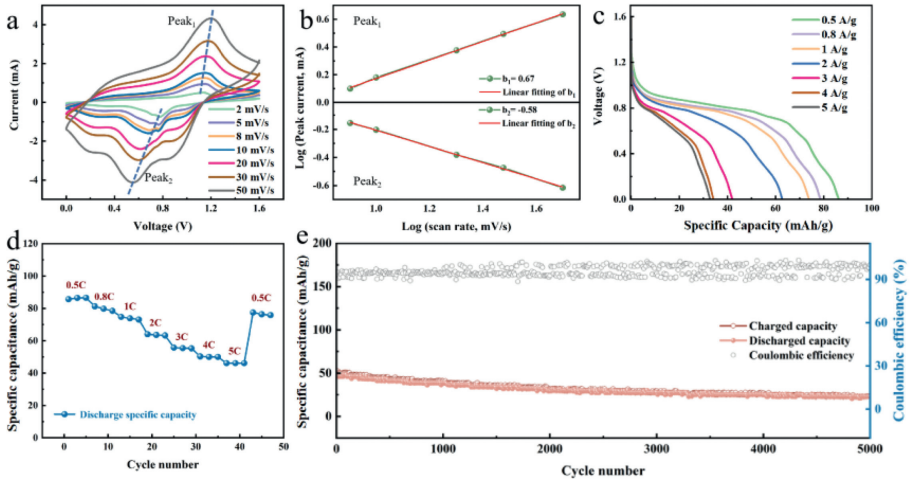


**Fig. 4.** Electrochemical properties of the BVO//CuHCF full cell. (a) CV curves at different scan rates. (b) log(*i*) *versus* log(*v*) plots of two redox peaks in CV curves. (c) Galvanostatic discharge curves at various current densities. (d) Rate performance between 0.5 C and 5 C. (e) Long-term cycling performance at the high current rate of 5 C.

In this case, *a* and *b* represent adjustable parameters, *i* represents the peak current and *v* represents the sweep rate. A score of $b = 1$ shows storage of charges based on capacitance, while a score of $b = 0.5$ is charge storage dominated by diffusion. The score of b can be obtained by linearly fitting log(*i*) and log(*v*). After fitting (Fig. 4b), the b-scores corresponding to the redox peak were 0.67 and 0.58, indicating it is possible to have capacitance control and diffusion-dominant charge storage simultaneously. Fig. 4c shows the performance of the rate of the BVO//CuHCF full cell. The BVO//CuHCF full cell delivers the specific capacities of 86.44, 79.76, 73.84, 63.57, 55.46, 50.03 mAh/g at 0.5, 0.8, 1, 2, 3, 4 as well as 5 C, accordingly. The charge capacity of the BVO//CuHCF whole cell was evaluated at different densities between 0.5 A/g and 5 A/g (Fig. 4d). When the current density is increased from 0.1 A/g to 5 A/g, the average output capability of BVO//CuHCF is reduced from 86.4 mAh/g to 46.1 mAh/g accordingly. Interestingly, even with a high score of 5 A/g, it still retains 53.3% of its capacity, with ten times the current density. Upon restoration of the current density to 0.5 A/g, the electrode is capable of recovering an average capability of 77.4 mAh/g, and the recovery rate is 89.7%. Fig. 4e indicates the long-term operation of the BVO//CuHCF whole cell at a high temp of 5 C. In order to further understand the mechanical stability of BVO anode and CuHCF cathode, SEM images were collected. Figs. S5 and S6 (Supporting information) show SEM images of the BVO anode and CuHCF cathode in their original state and deep cycling at 5 C. It can be seen that there are no obvious cracks on the surface of the BVO anode and CuHCF cathode, and the morphology of CuHCF in Fig. S5d is uniform. In Fig. S6d, BVO still maintains a good prism shape. The high structural stability of the electrode contributes to the increased strength of the battery and ensures the highly stable reversible capacity of AIBs [41]. Because of the excellent rate performance and cycle durability of the CuHCF cathode and the lubrication of BVO anode water ions, the BVO//CuHCF battery still has nearly 45% after 5000 cycles, showing the excellent cycle durability of the whole battery.

In summary, $Cu_3[Fe(CN)_6]_2$ was synthesized in this paper, demonstrating good cycle life (retaining 77% of the original capacity following 3500 cyclings) as well as good rate performance

(30-fold increase in current density can still maintain 74% capacity). A kind of barium vanadate was synthesized by hydrothermal method. The open frame structure could meet the requirement of ammonium ion embedded and dissociated, and the capacity was 138.54 mAh/g at 0.5 A/g. In order to construct AIBs, CuHCF was employed as the positive electrode, and BVO was used as the negative electrode to ensure that BVO//CuHCF has a good rate performance and long cycle life. The operating principle of AIBs was explained by *ex-situ* XRD, which has positive significance for the large-scale application of AIBs.

## Declaration of competing interest

The authors declare that they have no known competing financial interests or personal relationships that could have appeared to influence the work reported in this paper.

## Acknowledgments

This work was supported by Joint Funds of the National Natural Science Foundation of China (No. U22A20140), the Independent Cultivation Program of Innovation Team of Ji'nan City (No. 2019GXRC011), the Natural Science Foundation of Shandong Province, China (No. ZR2021MA073). All the authors discussed the results and commented on the manuscript.

## Supplementary materials

Supplementary material associated with this article can be found, in the online version, at doi:10.1016/j.cclet.2023.108449.

## References

[1] D. Larcher, J.M. Tarascon, Nat. Chem. 7 (2015) 19–29.
[2] C.Y. Wang, T. Liu, X.G. Yang, et al., Nature 611 (2022) 485–490.
[3] Z. Zhu, T. Jiang, M. Ali, et al., Chem. Rev. 122 (2022) 16610–16751.
[4] G. Xiang, Y. Meng, G. Qu, et al., Sci. Bull. 65 (2020) 443–451.
[5] B.E. Jia, A.Q. Thang, C. Yan, et al., Small 18 (2022) 2107773.
[6] X. Wang, X. Zhang, G. Zhao, et al., ACS Nano 16 (2022) 6093–6102.
[7] X. Zheng, Z. Liu, J. Sun, et al., Nat. Commun. 14 (2023) 76.
[8] M. Wang, J. Ma, Y. Meng, et al., Angew. Chem. Int. Ed. 62 (2023) e202214966.
[9] M. Wang, Y. Meng, K. Li, et al., eScience 2 (2022) 509–517.
[10] Z. Zhu, W. Wang, Y. Yin, et al., J. Am. Chem. Soc. 143 (2021) 20302–20308.
[11] R. Zhang, S. Wang, S. Chou, H. Jin, Adv. Funct. Mater. 32 (2022) 2112179.
[12] Q. Liu, F. Ye, K. Guan, et al., Adv. Energy Mater. 13 (2022) 2202908.
[13] M. Zhou, Y. Chen, G. Fang, S. Liang, Energy Storage Mater. 45 (2021) 618–646.
[14] L. Yan, Y.E. Qi, X. Dong, Y. Wang, Y. Xia, eScience 1 (2021) 212–218.
[15] J. Han, A. Varzi, S. Passerini, Angew. Chem. Int. Ed. 61 (2022) e202115046.
[16] S. Li, M. Xia, C. Xiao, et al., Dalton Trans. 50 (2021) 6520–6527.
[17] D. Yu, R. Tian, F. Du, Adv. Energy Sustain. Res. 3 (2022) 2100207.
[18] X. Zhang, M. Xia, T. Liu, et al., Chem. Eng. J. 421 (2021) 127767.
[19] Y. Wu, S. Dong, N. Lv, et al., Small 18 (2022) 2204888.
[20] S. Dong, W. Shin, H. Jiang, et al., Chem 5 (2019) 1537–1551.
[21] X. Wu, Y. Qi, J.J. Hong, et al., Angew. Chem. Int. Ed. 56 (2017) 13026–13030.
[22] Z. Li, T. Liu, R. Meng, et al., Energy Environ. Mater. 4 (2021) 111–116.
[23] S. Qiu, Y. Xu, X. Wu, X. Ji, Energy Rev. 5 (2022) 242–262.
[24] W.J. Li, C. Han, G. Cheng, et al., Small 15 (2019) 1900470.
[25] Y. Yang, J. Zhou, L. Wang, et al., Nano Energy 99 (2022) 107424.
[26] Y. Gao, H. Yang, X. Wang, et al., ChemSusChem 13 (2020) 732–740.
[27] L. Jiang, Y. Lu, C. Zhao, et al., Nat. Energy 4 (2019) 495–503.
[28] Y. Song, Q. Pan, H. Lv, et al., Angew. Chem. Int. Ed. 60 (2021) 5718–5722.
[29] J. Zhu, X. Chen, A.Q. Thang, et al., SmartMat 3 (2022) 384–416.
[30] T. Zhou, Q. Han, L. Xie, et al., Chem. Rec. 22 (2022) e202100275.
[31] X. Chen, P. Wang, Z. Feng, C. Meng, Y. Zhang, Chem. Eng. J. 445 (2022) 136747.
[32] W. Deng, Z. Zhou, Y. Li, et al., ACS Nano 14 (2020) 15776–15785.
[33] X. Wang, B. Xi, X. Ma, et al., Nano Lett. 20 (2020) 2899–2906.
[34] C. Wang, S. Zhao, X. Song, et al., Adv. Energy Mater. 12 (2022) 2200157.
[35] T. Wang, S. Zhao, G. Qu, J. Leng, X. Xu, J. Colloid Interface Sci. 615 (2022) 293–301.
[36] C. Zhang, X. Liu, Z. Li, et al., Adv. Funct. Mater. 31 (2021) 2101470.
[37] O. Okhay, A. Tkach, Nanomaterials 11 (2021) 1240.
[38] S. Geng, T. Zhou, M. Jia, et al., Energy Environ. Sci. 14 (2021) 3184–3193.
[39] Y. Yang, P. Zhang, L. Hao, et al., Angew. Chem. Int. Ed. 133 (2021) 22009–22016.
[40] X. Guan, J. Chen, E. Zhu, et al., J. Mater. Sci. Technol. 150 (2023) 145–158.
[41] C. Li, G. Qu, X. Zhang, C. Wang, X. Xu, Energy Environ. Mater. (2023), doi:10.1002/eem2.12608.